



Research paper

Hyperspectral image mixed noise removal via jointly spatial and spectral difference constraint with low-rank tensor factorization

Qiang Zhang^a, Yaming Zheng^a, Yushuai Dong^a, Chunyan Yu^{a,*}, Qiangqiang Yuan^b^a Center of Hyperspectral Imaging in Remote Sensing (CHIRS), Information Science and Technology College, Dalian Maritime University, Dalian, China^b School of Geodesy and Geomatics, Wuhan University, Wuhan, China

ARTICLE INFO

Keywords:

Hyperspectral image (HSI)
Artificial intelligence
Mixed noise removal
Spatial-spectral difference
Low-rank tensor factorization
Local smoothness
Global correlation

ABSTRACT

The denoising of hyperspectral image (HSI) plays a crucial role in the subsequent interpretation and application. The rise of artificial intelligence technology has brought new opportunities for hyperspectral image denoising, and its potential and advantages in this field are gradually changing the traditional denoising pattern. This paper proposes a jointly spatial and spectral difference constraints with low-rank tensor factorization. Firstly, the spatial and spectral difference is combined in the framework of low-rank tensor factorization, to fully mine global spatial-spectral information and improve the removal ability of complex distribution noise. Secondly, based on the premise of effectively preserving HSI intrinsic three-dimensional structure, the spatial horizontal and vertical difference constraints are used to mine the local smoothness and similarity of spatial. Thirdly, the full-band spectral difference constraint could not only characterize the continuity and sparsity of the whole spectral domain, but also effectively characterize the noise distribution with linear structure. Finally, experiments on simulated and real HSIs show that the proposed method outperforms state-of-the-art methods in removing mixed noise performance.

1. Introduction

Hyperspectral images (HSIs) are obtained through hyperspectral sensors, which capture various electromagnetic wave signals from the ultraviolet, visible, to infrared bands. These spectrums are continuous and typically have narrow spectral intervals (Dian et al., 2020; Wang et al., 2024). The HSI captures a wealth of spatial and spectral information regarding the observed objects. By means of the continuous spectral curves, HSI could effectively differentiate the physical characteristics of various surface materials, making it widely applicable in numerous fields, including classification (Yu et al., 2022a, 2024; Ahmad et al., 2024), change detection (Jie Zhang and wei Liu, 2024), and others (Zhang et al., 2021c; Yu et al., 2022b; Xiao et al., 2022; Zheng et al., 2021).

However, due to the sensitivity of sensors, imaging mechanisms, circuit signal responses, and atmospheric interference, almost all the acquired HSIs are inherently subject to contamination from different types of noise, including Gaussian, stripe, deadline, mixed noise. If we discard the noisy HSIs, it would result in a serious loss of valuable data (Zhang et al., 2021b; Gao et al., 2022). However, if we ignore the issue of noise contamination and directly utilize the noisy HSI in subsequent applications, it is likely to bring about a detrimental impact for interpretation (Zhang et al., 2018, 2020b; Xiao et al., 2023b; Yu

et al., 2023). For instance, numerous studies have demonstrated that noise contamination significantly diminishes the classification accuracy of HSI (Zhang et al., 2023b; Xu et al., 2024; Chen et al., 2018a). Therefore, denoising is a crucial pre-processing procedure to improve the quality of hyperspectral images. Generally, hardware-based approaches usually struggle to remove mixed noise from HSI (Kerekes and Baum, 2003; Xiao et al., 2023a). On the contrary, software algorithms offer a viable alternative for noise removal in HSI (Zhang et al., 2023a, 2019, 2020c, 2022b).

So far, a mass of HSI denoising methods have been developed. These methods could be divided into three types: model-driven (Su et al., 2023; Chen et al., 2018b; Fu et al., 2023; Li et al., 2023), data-driven (Miao et al., 2022; Wang et al., 2022) and model-data-driven methods (Xiong et al., 2022b; Zhang et al., 2021a).

Model-driven methods are designed to use mathematical models (Fernandes et al., 2020; Wu et al., 2024; He et al., 2024; Ma et al., 2020; Wang et al., 2018; Huang et al., 2024; Zhang et al., 2020a; Pan et al., 2024) and prior knowledge for modeling and processing HSI. For instance, to fully exploit the spatial structural information in HSI, He et al. (2015) developed an approach that combines total variation regularization with low rank matrix representation. This approach considers

* Corresponding author.

E-mail address: yucy@dltu.edu.cn (C. Yu).

both the smoothness of the image and the global structure. Peng et al. (2022a) proposed a regularizer called Representative Coefficient Total Variation, which could capture both low-rankness and smoothness, thereby achieving fast removal of noise. To excavate the spectrum low-rank property of HSI, He et al. (2019) utilized the Tucker-3 tensor decomposition method for HSI denoising. However, mining information from a single dimension cannot achieve high-quality denoising effects. Therefore, it is crucial to consider spatial-spectral dimensions of the information on denoising task. To address this issue, Peng et al. (2020) introduced an enhanced 3D total variation model. By applying 3-D total variation regularization, this method captures the sparse characteristic of HSI. In addition, Zhang et al. (2022a) developed an approach based on hybrid space-spectrum total variation (SSTV) regularization, which is called ℓ_0 - ℓ_{1-2} SSTV. Specifically, it can be regarded as an ensemble regularization of the spatial-spectral gradient model into the SSTV. Jiang et al. (2022) developed a new hybrid noise removal method for HSIs. It takes into account the inherent low-rank and self-similarity of HSI. Subsequently, Sun et al. (2023a) constructed a hybrid prior model of global tensor low-rank and non-local group sparsity. Zhuang and Ng (2023) proposed an efficient and parameter-free hybrid denoising approach for HSI that utilizes a Gaussian mixture model to depict the intricate distribution of noise.

Data-driven methods have experienced a rapid development in recent years. These approaches are designed to discover the non-linear correlation between noisy and clean HSIs. For instance, Pan et al. (2022) developed an end-to-end model based on encoder-decoder architecture and quasi attention mechanism. This model effectively extracts both spatial and spectral information from HSI. Wei et al. (2020) introduced a 3D quasi-recurrent neural network, which combines three-dimensional CNN and recursive neural networks. This method explores the spectral global low-rank and spatial self-similarity to remove noise in HSI. Wang et al. (2023a) proposed an LL1 decomposition based on nonlinear learnable transformation (NT-LL1) to characterize the low-rank structure of HSI. Luo et al. (2021) constructed an unsupervised spatial-spectral deep image prior (S2DIP), which utilizes the spatial-spectral features to facilitate HSI restoration.

In HSI denoising field, model-data-driven algorithms are gradually becoming the hot topic. For example, Zhang et al. (2020c) introduced a Deep Spatio-Spectral Bayesian Posterior model. This model executes noise assessment within a Bayesian structure, and it fuses three convolutional sub-networks with this Bayesian structure to learn the trainable parameters. Zhang et al. (2021a) introduced a low-rank spatio-spectral network for HSI mixing noise removal. The network embeds the low-rank prior into the convolutional framework. Xiong et al. (2022a) proposed the subspace based multi-dimensional sparse network aimed to remove HSI noise. This approach embeds low-rank and sparsity into convolutional network.

On one hand, model-driven methods still face challenges when dealing with the HSI mixing noise. For the complexity of mixing noise, it is difficult to establish accurate model to describe and separate the noise components. These methods not only require modeling the characteristics of different types of noise, but also involve a large amount of time and effort for tuning the model parameters.

On the other hand, data-driven methods aim to fit the noise distribution by training labels and samples, and perform noise removal on this basis. However, when the noise in HSI exhibits a complex and high-intensive distribution, most data-driven methods are hard to accurately model such mixed noise distribution. This issue may lead to overfitting issues, resulting in poor denoising performance.

Furthermore, model-data-driven approaches sidestep the issues of laborious parameter tuning and scarcity of training data. Nevertheless, its capacity to generalize is not reliable across various noisy HSIs.

To solve aforementioned problems, this paper proposes a novel method named jointly spatial and spectral difference constraint with low-rank tensor factorization (JSSDC-LRTF), to remove HSI mixed noise. The innovations of this method are listed as follows.

- This paper combines spatial difference and spectral difference regularization constraint within the framework of low-rank tensor factorization. The three-dimensional spatial-spectral information is fully utilized to improve the ability to remove complex distribution noise.
- Building upon the preservation of the inherent three-dimensional structural information in HSI, spatial difference constraint on the horizontal and vertical dimensions are used to mine local smoothness and similarity of spatial information. The full-band spectral difference constraint could not only retain the original spectral information well and better characterize the continuity, sparsity and global correlation of the spectrum, but also better characterize the noise distribution with linear structure by calculating the difference between adjacent bands.
- In simulated and real datasets experiments, the proposed method could show more excellent recovery effects over the SOTA methods in removing mixed noise, particularly for high intensity and dense mixed noise.

The remaining part of this paper is organized as follows. Section 2 presents the notations and preliminaries. Section 3 introduces the proposed model. Section 4 provides relevant simulated and real experiments, as well as an analysis of the sensitivity of model parameters. Finally, Section 5 concludes the paper, providing a summary of the work.

2. Related work

In this paper, we use lowercase Times New Roman letters to represent scalars, uppercase boldface Times New Roman letters to represent vectors and matrixes, and Euclidean mathematical font to represent tensors. For an N-order tensor $\mathcal{X} \in \mathbb{R}^{I_1 \times I_2 \times \dots \times I_N}$ and matrix $\mathbf{X} \in \mathbb{R}^{J_n \times I_n}$, the mode-n tensor-matrix product is represented as $\mathcal{Y} = \mathcal{X} \times_n \mathbf{A}$, where $\mathcal{Y} \in \mathbb{R}^{I_1 \times \dots \times I_{n-1} \times J_n \times I_{n+1} \times \dots \times I_N}$. The inner product of two matrices of the same dimension is represented as $\langle \mathbf{X}, \mathbf{Y} \rangle = \sum_{i,j} x_{i,j} \cdot y_{i,j}$. Mode-n unfolding matrix of tensor \mathcal{X} is denoted as $\mathbf{X}_{(n)} = \text{unfold}_n(\mathcal{X}) \in \mathbb{R}^{I_n \times (I_1 \times \dots \times I_{n-1} \times I_{n+1} \times \dots \times I_N)}$, and $\text{fold}_n(\mathbf{X}_{(n)}) = \mathcal{X}$, where fold_n is the inverse of unfold operator. Frobenius and ℓ_1 norms are represented as $\|\mathbf{X}\|_F = (\langle \mathbf{X}, \mathbf{X} \rangle)^{1/2}$ and $\|\mathbf{X}\|_1 = \sum_{i,j} |x_{i,j}|$, respectively.

HSI can be regarded as three-order tensor $\mathcal{X} \in \mathbb{R}^{M \times N \times P}$. It can also be represented as a dimensionality reduction matrix $\mathbf{X} \in \mathbb{R}^{MN \times P}$. This matrix exhibits a strong low-rank property, where the rank r is significantly smaller than the dimensionality P of the matrix. And the columns of this matrix constitute the vectorized spectral bands of the HSI.

2.1. Tucker decomposition

Low-rank tensor decomposition can effectively extract and utilize redundant information, so as to achieve effective noise removal. In addition, as a three-dimensional data cube, the hyperspectral image contains rich spatial and spectral information, and the tensor decomposition method can naturally deal with this multi-dimensional data structure and retain the global structure and intrinsic correlation of the image. A tucker decomposition of a third-order tensor form is as follows (Sun and He, 2021):

$$\mathcal{X} \approx \mathcal{G} \times_1 \mathbf{A} \times_2 \mathbf{B} \times_3 \mathbf{C} = \sum_{p=1}^P \sum_{q=1}^Q \sum_{r=1}^R g_{pqr} \mathbf{a}_p \circ \mathbf{b}_q \circ \mathbf{c}_r = [\mathcal{G}; \mathbf{A}, \mathbf{B}, \mathbf{C}] \quad (1)$$

where $\mathbf{A} \in \mathbb{R}^{I \times P}$, $\mathbf{B} \in \mathbb{R}^{J \times Q}$, $\mathbf{C} \in \mathbb{R}^{K \times R}$ are the factor matrixes obtained from the Tucker decomposition. $\mathcal{G} \in \mathbb{R}^{P \times Q \times R}$ represents the core tensor. \circ represents the product between the elements of the matrix, also known as the Hadamard product. Different tucker decomposition modes reflect different levels of interaction between factor matrixes. And its Tucker-3 decomposition form is $\mathcal{X} \approx \mathbf{B} \times_3 \mathbf{A}$. \mathbf{B} is the spatial reduced image, \mathbf{A} represents the spectral subspace matrix.

2.2. Total variation regularization

The Total Variation regularization was originally developed by Rudin et al. (1992), due to its ability to effectively preserve edge information and enhance smoothness. TV regularization has been widely used in image denoising problems (Beck and Teboulle, 2009). For a 2D image \mathbf{X} of size $M \times N$, the anisotropic TV norm is represented below:

$$\|\mathbf{X}\|_{TV} = \sum_{i=1}^{M-1} \sum_{j=1}^{N-1} \left\{ |x_{i,j} - x_{i+1,j}| + |x_{i,j} - x_{i,j+1}| \right\} + \sum_{i=1}^{M-1} |x_{i,N} - x_{i+1,N}| + \sum_{j=1}^{N-1} |x_{M,j} - x_{M,j+1}| \quad (2)$$

It can be written as:

$$\|\mathbf{X}\|_{TV} = \|D_h \mathbf{X}\|_1 + \|D_v \mathbf{X}\|_1 \quad (3)$$

where D_h and D_v are the first-order difference operators in the horizontal and vertical dimensions.

Each band of HSI can be seen as a gray image. Therefore, we can individually apply the TV norm to each band of the HSI. Afterward, the norms of each band are summed up. The TV norm for each band is defined below (Yao et al., 2019):

$$\|\mathbf{X}\|_{HTV} = \sum_{j=1}^p \|\mathcal{F} \mathbf{X}_j\|_{TV} \quad (4)$$

where \mathbf{X}_j represents the vector of the HSI j th band. $\mathcal{F} : \mathbb{R}^{MN} \rightarrow \mathbb{R}^{M \times N}$ denotes the operator that reconstructs the j th band vector into the $M \times N$ image.

2.3. Gradient tensor

The gradient tensor of $\mathcal{X} \in \mathbb{R}^{n_1 \times n_2 \times \dots \times n_d}$ with respect to mode- k is defined as in Wang et al. (2023b):

$$\mathcal{G}_k = \nabla_k(\mathcal{X}) = \mathcal{X} \times_k \mathbf{D}_{n_k}, k = 1, 2, \dots, d \quad (5)$$

where \mathbf{D}_{n_k} is a row-circulant matrix.

3. Methodology

The observed HSI $\mathcal{Y} \in \mathbb{R}^{M \times N \times P}$ is typically contaminated by mixed noise. The spatial dimension is denoted as $M \times N$, and the spectral dimension is denoted as P . The mixed noise includes Gaussian, deadline, stripe noise. HSI contaminated by mixed noise can be approximated as an additive degradation process:

$$\mathcal{Y} = \mathcal{X} + \mathcal{N} + \mathcal{S} \quad (6)$$

where $\mathcal{X} \in \mathbb{R}^{M \times N \times P}$ represents the clean HSI. $\mathcal{N} \in \mathbb{R}^{M \times N \times P}$ represents random noise, such as Gaussian and Poisson. $\mathcal{S} \in \mathbb{R}^{M \times N \times P}$ represents sparse noise, for example stripe and deadline. The objective of HSI denoising is to reconstruct the noise-free HSI \mathcal{X} from the noisy HSI \mathcal{Y} .

In accordance with linear spectral mixing model, every spectral signature within HSI could be depicted as a linear aggregate of a few endmember spectra (Yao et al., 2019). However, due to the pronounced correlations among the spectral bands within HSI, low-rank matrix decomposition model is employed to depict HSI as $\mathbf{X} = \mathbf{U}\mathbf{V}^T$. Here, $\mathbf{U} \in \mathbb{R}^{MN \times r}$ ($r \ll P$) represents the abundance map. $\mathbf{V} \in \mathbb{R}^{P \times r}$ denotes the endmember matrix. Thus, the degradation model can be expressed as:

$$\mathbf{Y} = \mathbf{U}\mathbf{V}^T + \mathbf{N} + \mathbf{S} \quad (7)$$

where \mathbf{Y} , \mathbf{N} , and \mathbf{S} are matrixes after the dimensionality reduction of \mathcal{Y} , \mathcal{N} , and \mathcal{S} in Eq. (6), respectively.

We apply the TV constraint to each slice of the tensor $\mathcal{X} \in \mathbb{R}^{M \times N \times P}$, thereby constructing a jointly spatial and spectral difference regularization constraint. This procedure can be divided into two steps: the initial

step involves spatial difference regularization, while the subsequent step involves spectral difference regularization.

For a third-order tensor $\mathcal{X} \in \mathbb{R}^{M \times N \times P}$, we define the jointly spatial and spectral difference constraint with low-rank tensor factorization regularization constraint as follows:

$$\|\mathcal{X}\|_{JSSDC-LRTF} = \sum_{i=1}^M \sum_{j=1}^N \|\mathcal{X}(i, j, :) \|_{TV} + \sum_{k=1}^P \|\mathcal{U}(:, :, k)\|_{TV} \quad (8)$$

where $\mathcal{U} = \mathcal{X} \times_3 \mathbf{V}$, and $\mathbf{V} \in \mathbb{R}^{P \times r}$ is an endmember matrix. The tensor $\mathcal{U} \in \mathbb{R}^{M \times N \times r}$ can be dimensionally reduced to the matrix $\mathbf{U} \in \mathbb{R}^{MN \times r}$. To simplify the notation, this paper defines the spatial and spectral difference as follows:

$$\nabla_1(\mathbf{U}) = [D_h \mathcal{U}(:, :, 1), \dots, D_h \mathcal{U}(:, :, r)],$$

$$\nabla_2(\mathbf{U}) = [D_v \mathcal{U}(:, :, 1), \dots, D_v \mathcal{U}(:, :, r)],$$

$$\nabla_3(\mathcal{X}) = [D_B \mathcal{X}(1, 1, :), \dots, D_B \mathcal{X}(M, N, :)]$$

where $\nabla_1(\mathbf{U})$, $\nabla_2(\mathbf{U})$ and $\nabla_3(\mathcal{X})$ represent the spatial horizontal difference, the spatial vertical difference and the spectral difference, respectively. Thus, we can express the JSSDC-LRTF regularization below:

$$\|\mathcal{X}\|_{JSSDC-LRTF} = \|\nabla_1(\mathbf{U})\|_1 + \|\nabla_2(\mathbf{U})\|_1 + \|\nabla_3(\mathcal{X})\|_1 \quad (10)$$

3.1. Model proposal

In this section, we develop an approach to remove HSI mixing noise. The flowchart is illustrated in Fig. 1 and can be divided into four steps:

(a) Tensor decomposition: The HSI is decomposed into coefficient image \mathcal{A} and endmember matrix \mathbf{B} via the Tucker mode-3 tensor decomposition, as depicted in Eq. (1).

(b) Spatial difference: The coefficient image \mathcal{A} undergoes spatial difference operation, to obtain two-dimensional spatial difference images for each band in \mathcal{A} . These difference results are then stacked and reconstructed to obtain the spatial difference image \mathcal{A}' , as shown in Eq. (3).

(c) Spectral difference: The spatial difference image \mathcal{A}' is multiplied with the endmember matrix \mathbf{B} using the Tucker mode-3 tensor-matrix product, resulting in the image $\mathcal{A}' \times_3 \mathbf{B}$. Subsequently, spectral difference operation is applied to obtain the spectral difference tensor, as depicted in Eq. (9).

(d) Iterative optimization: The spectral difference tensor is subjected to a fast Fourier transform (FFT), resulting in the reconstructed HSI. Subsequently, an iterative optimization process is performed using alternating direction method of multipliers approaches to refine final restored HSI.

In real HSIs, the distribution and types of noise are usually complex. Different types of noise may interact with each other. Here, we utilize the ℓ_1 -norm to describe the sparse noise component and the ℓ_2 -norm to describe the Gaussian noise component. Based on the definition (10), we developed a denoising approach base on JSSDC-LRTF regularization as below:

$$\min_{\mathbf{A}, \mathbf{B}, \mathcal{X}, \mathcal{N}, \mathcal{S}} \sum_{i=1}^2 \tau_i \|\nabla_i(\mathbf{A})\|_1 + \tau_3 \|\nabla_3(\mathcal{X})\|_1 + \beta \|\mathcal{N}\|_F^2 + \lambda \|\mathcal{S}\|_1 \quad (11)$$

$$\text{s.t. } \mathcal{Y} = \mathcal{X} + \mathcal{N} + \mathcal{S}, \mathcal{X} = \mathcal{A} \times_3 \mathbf{B}, \mathbf{I} = \mathbf{B}^T \mathbf{B}$$

where the dimensionality reduction matrix \mathbf{A} corresponds to \mathbf{U} as defined in Eq. (7). \mathbf{B} corresponds to \mathbf{V} , where \mathbf{V} is an endmember matrix. Here, it is orthogonal. $\tau_{1,2,3}, \beta, \lambda$ are the tuning parameters employed to regulate the weights of different terms.

3.2. Model optimization

We introduce auxiliary variables $\mathbf{G}_1, \mathbf{G}_2, \mathbf{G}_3$ and rewrite (11) as follows:

$$\arg \min_{\mathbf{A}, \mathbf{B}, \mathcal{X}, \mathcal{N}, \mathcal{S}} \sum_{i=1}^2 \tau_i \|\mathbf{G}_i\|_1 + \tau_3 \|\mathbf{G}_3\|_1 + \beta \|\mathcal{N}\|_F^2 + \lambda \|\mathcal{S}\|_1 \quad (12)$$

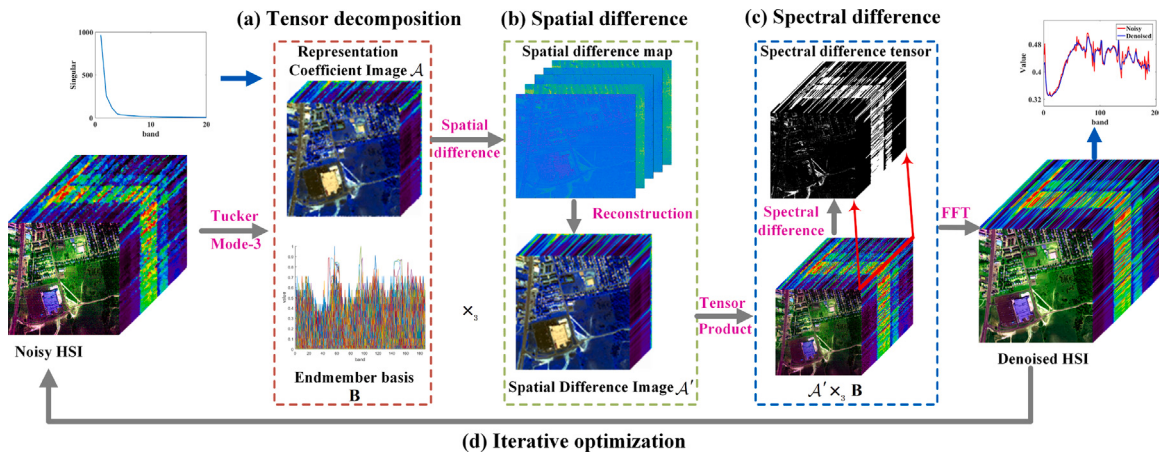


Fig. 1. Flowchart of the proposed method. The method can be divided into four steps: (a) Tensor decomposition; (b) Spatial difference; (c) Spectral difference; and (d) Iterative optimization.

where $\nabla_i(\mathbf{A})$ is equal to \mathbf{G}_i , and $\nabla_3(\mathcal{X})$ is equal to \mathcal{G}_3 in (11).

Next, we utilize the ADMM algorithm to find the optimal solution for Eq. (12). The augmented Lagrange function for Eq. (12) is given below:

$$\begin{aligned} \mathcal{L}(\mathbf{A}, \mathbf{B}, \mathcal{X}, \mathcal{N}, \mathcal{S}, \{\mathbf{G}\}_{i=1}^2, \mathcal{G}_3, \{\Gamma_i\}_{i=1}^4) \\ := \sum_{i=1}^2 \tau_i \|\mathbf{G}_i\|_1 + \frac{\mu}{2} \sum_{i=1}^2 \left\| \nabla_i(\mathbf{A}) - \mathbf{G}_i + \frac{\Gamma_i}{\mu} \right\|_F^2 \\ + \tau_3 \|\mathcal{G}_3\|_1 + \frac{\mu}{2} \left\| \nabla_3(\mathcal{X}) - \mathcal{G}_3 + \frac{\Gamma_3}{\mu} \right\|_F^2 + \beta \|\mathcal{N}\|_F^2 \\ + \lambda \|\mathcal{S}\|_1 + \frac{\mu}{2} \left\| \mathcal{Y} - \mathcal{X} - \mathcal{N} - \mathcal{S} + \frac{\Gamma_4}{\mu} \right\|_F^2 \end{aligned} \quad (13)$$

where μ is the penalty parameter. Γ_i are the Lagrange multipliers. Subsequently, we must solve the local optimal solution of the subvariate.

Updating \mathbf{G}_i :

$$\arg \min_{\mathbf{G}_i} \tau_i \|\mathbf{G}_i\|_1 + \frac{\mu}{2} \left\| \nabla_i(\mathbf{A}) - \mathbf{G}_i + \frac{\Gamma_i}{\mu} \right\|_F^2 \quad (14)$$

It is obtained by using the soft threshold operator \mathcal{S} :

$$\mathbf{G}_i = \mathcal{S}_{\tau_i/\mu} (\nabla_i(\mathbf{A}) + \Gamma_i/\mu) \quad (15)$$

Updating \mathcal{G}_3 :

$$\arg \min_{\mathcal{G}_3} \tau_3 \|\mathcal{G}_3\|_1 + \frac{\mu}{2} \left\| \nabla_3(\mathcal{X}) - \mathcal{G}_3 + \frac{\Gamma_3}{\mu} \right\|_F^2 \quad (16)$$

By employing the third-order tensor singular value thresholding (t-SVT) (Qin et al., 2022), it is calculated as:

$$\mathcal{G}_3 = \text{t-SVT}_{\tau_3/\mu} (\nabla_3(\mathcal{X}) + \Gamma_3/\mu) \quad (17)$$

Updating endmember matrix \mathbf{B} :

$$\arg \max_{\mathbf{B}} \left\langle (\mathbf{Y} - \mathbf{N} - \mathcal{S} + \Gamma_4/\mu)^T \mathbf{A}, \mathbf{B} \right\rangle \quad (18)$$

Using Singular Value Decomposition (SVD), we can solve Eq. (18) as follows:

$$\begin{cases} [\mathbf{H}, \mathbf{J}, \mathbf{K}] = \text{SVD} \left((\mathbf{Y} - \mathbf{N} - \mathcal{S} + \Gamma_4/\mu)^T \mathbf{A} \right) \\ \mathbf{B} = \mathbf{J} \mathbf{K}^T \end{cases} \quad (19)$$

Updating coefficient image \mathbf{A} :

$$\left(\mu \mathbf{I} + \mu \sum_{i=1}^2 \nabla_i^T \nabla_i \right) (\mathbf{A}) = \mu (\mathbf{Y} - \mathbf{N} - \mathcal{S} + \Gamma_4/\mu) \mathbf{V} + \sum_{i=1}^2 \nabla_i^T (\mu \mathbf{G}_i - \Gamma_4) \quad (20)$$

It can be solved via FFT. Specifically, by performing a Fourier transform and applying the convolution theorem, we can derive the

closed-form solution for \mathbf{A} as (Krishnan and Fergus, 2009):

$$\begin{cases} \mathbf{H} = \sum_{i=1}^2 \mathcal{F}(\mathbf{D}_i)^* \odot \mathcal{F} \left(\text{fold} \left(\mu \mathbf{G}_i \right) - \Gamma_i \right) \\ \mathbf{T}_x = |\mathcal{F}(\mathbf{D}_1)|^2 + |\mathcal{F}(\mathbf{D}_2)|^2 \\ \mathbf{A} = \mathcal{F}^{-1} \left(\frac{\mathcal{F} \left(\text{fold} \left(\mu (\mathbf{Y} - \mathbf{N} - \mathcal{S}) + \Gamma_3 \right) + \mathbf{H} \right)}{\mu \mathbf{1} + \mu \mathbf{T}_x} \right) \end{cases} \quad (21)$$

where $|\cdot|^2$ represents the element-wise square operator. \odot stands for the product of each element. $\mathbf{1}$ denotes matrix with all elements 1.

Updating recovered image \mathcal{X} :

$$(\mathbf{I} + \nabla_3^T \nabla_3) (\mathcal{X}) = (\mathbf{Y} - \mathbf{N} - \mathcal{S} + \Gamma_4/\mu) + \nabla_3^T (\mathcal{G}_3 - \Gamma_4) \quad (22)$$

According to the convolution theorem of the Fourier transform, the optimal solution of (22) is obtained as:

$$\begin{cases} \mathcal{H} = \mathcal{F}(\mathcal{D}_3)^* \odot \mathcal{F}(\mathcal{G}_3 - \Gamma_4) \\ \mathcal{X} = \mathcal{F}^{-1} \left(\frac{\mathcal{F} \left(\mathbf{Y} - \mathbf{N} - \mathcal{S} + \Gamma_4/\mu \right) + \mathcal{H}}{1 + \mathcal{F} \mathcal{D}_3^* \odot \mathcal{F} \mathcal{D}_3} \right) \end{cases} \quad (23)$$

Updating Gaussian noise \mathcal{N} :

$$\mathcal{N} = (\mu(\mathbf{Y} - \mathcal{X} - \mathcal{S}) + \Gamma_4)/(\mu + 2\beta) \quad (24)$$

Updating Gaussian noise \mathcal{S} :

$$\mathcal{S} = \mathcal{S}_{\lambda/\mu} (\mathbf{Y} - \mathcal{X} - \mathcal{N} + \Gamma_4/\mu) \quad (25)$$

Updating Lagrange multipliers Γ_i :

$$\begin{cases} \Gamma_{1,2} = \Gamma_{1,2} + \mu \nabla_{1,2} \mathbf{A} - \mathbf{G}_{1,2} \\ \Gamma_3 = \Gamma_3 + \mu \nabla_3 \mathcal{X} - \mathcal{G}_3 \\ \Gamma_4 = \Gamma_4 + \mu \mathbf{Y} - \mathcal{X} - \mathcal{N} - \mathcal{S} \end{cases} \quad (26)$$

Based on above discussions, the optimized workflow is summarized in Algorithm 1. And the overall computational cost of the proposed algorithm is: $O((P+r)MN \log(MN) + MNP + r^2P)$.

Algorithm 1 JSSDC-LRTF Solver

Input: HSI data $\mathcal{Y} \in \mathbb{R}^{M \times N \times P}$, hyper-parameter $\tau = 0.8$, $\lambda = 2$, $\beta = 80$ and rank $r = 4$.

Initialization: Initialize $\mu = 1e-4$, $\varepsilon = 1e-6$. $SVD(\mathcal{Y}) = [\mathbf{U}, \mathbf{O}, \mathbf{B}]$, $\mathbf{A} = \mathbf{U}_r \mathbf{O}_r$, $\mathbf{B} = \mathbf{B}_r$.

$\mathbf{U}_r, \mathbf{O}_r, \mathbf{B}_r$ are the first r vectors of $\mathbf{U}, \mathbf{O}, \mathbf{B}$.

1: while not converge do

2: Update variables

$$\mathbf{G}_{1,2}, \mathcal{G}_3, \mathbf{A}, \mathbf{B}, \mathcal{X}, \mathcal{N}, S. \text{ by Eqs. (15), (17), (19), (21), (23), (24), (25).}$$

3: Update $\Gamma_{1,2,3,4}$ by Eq. (26).

4: Check the convergence conditions

$$\begin{aligned} & \|\mathcal{Y} - \mathcal{X} - \mathcal{N} - S\|_F^2 / \|\mathcal{Y}\|_F^2 \leq \varepsilon \\ & \|\nabla_i \mathbf{A} - \mathbf{G}_i\|_F^2 / \|\mathbf{Y}\|_F^2 \leq \varepsilon, i = 1, 2 \\ & \|\nabla_3 \mathcal{X} - \mathcal{G}_3\|_F^2 / \|\mathcal{Y}\|_F^2 \leq \varepsilon \end{aligned}$$

5: end while

Output: Reconstructed HSI \mathcal{X} .

In hyperspectral image denoising, the convergence condition is often used to measure the stability and effectiveness of the algorithm. The first convergence condition $\|\mathcal{Y} - \mathcal{X} - \mathcal{N} - S\|_F^2 / \|\mathcal{Y}\|_F^2 \leq \varepsilon$ is used to ensure that the difference between the denoised image and the clean image is within an acceptable range.

The second convergence condition $\|\nabla_i \mathbf{A} - \mathbf{G}_i\|_F^2 / \|\mathbf{Y}\|_F^2 \leq \varepsilon, i = 1, 2$ is used to ensure that the difference between the spatial gradient information in the denoising process and the spatial gradient information of the clean image is within an acceptable range.

The third convergence condition $\|\nabla_3 \mathcal{X} - \mathcal{G}_3\|_F^2 / \|\mathcal{Y}\|_F^2 \leq \varepsilon$ is used to ensure that the difference between the spectral gradient information in the denoising process and the spectral gradient information of the clean image is within the acceptable range. Ideally, the numerator of the three constraints is equal to 0, and the denominator uses the original image to normalize the difference and reduce the difference before and after denoising. However, since it is not possible to completely remove the noise, we set the convergence value to a reasonably small value close to 0 (in this case, it is set to). If the setting is too small, it is easy to overfit. And if the setting is too large, it will cause underfitting with insufficient noise removal.

4. Experiments and results

To prove the effectiveness of the developed approach, we conduct simulation and real HSI denoising experiments in this section.

For comparative methods, we select eight HSI denoising methods. These methods could be categorized into four groups. Specifically, for low-rank prior based methods, we chose STCR (Sun et al., 2023b). For coefficient matrix-based methods using nonlocal similarity prior modeling, we select NGMeet (He et al., 2019). For models founded on combine low-rank and local smoothness, we use stable denoising methods such as LRTV (He et al., 2015), CTV-RPCA (Peng et al., 2022b) and RCTV (Peng et al., 2022a). For data-driven methods, we employ HSID (Yuan et al., 2019), MAN (Lai and Fu, 2023) and QRNN3D (Wei et al., 2020). Regarding the parameter settings of these comparative methods, we fine-tune them based on the default setting to ensure the optimal performance.

In terms of evaluation metrics for the simulation experiments, we select three quantitative indices: Mean Peak Signal-to-Noise Ratio (MP-SNR), Mean Structural Similarity (MSSIM), and Error Relative Global Accuracy Synthesis (ERGAS). MPSNR and MSSIM represent the average values of PSNR and SSIM, respectively, calculated for each spectral band. PSNR and SSIM are spatial domain-based quantitative evaluation standards. ERGAS is a spectral domain-based quantitative evaluation standard. Higher values of MPSNR and MSSIM indicate better quality of the reconstructed HSI. While a lower value of ERGAS indicates better

quality of the reconstructed HSI. We normalize the grayscale values of the HSI and adjust them on a per-band basis to the range [0, 1].

For the hardware platform of the experiments, the model-driven methods are tested on a computer equipped with an Intel i9-12900H CPU. On the other hand, the data-driven methods are tested on a computer with an Intel i9-12900K CPU and an RTX 4090 GPU.

4.1. Simulation experiments

For the dataset, we select the noise-free HSI data of Washington D.C. Mall for the comparative experiments. In the simulation experiments, we perform size cropping on the Washington D.C. Mall data, resulting in a data size of $256 \times 256 \times 191$. The noise types include Gaussian, stripe and deadline noise, which are mixed to simulate a noisy dataset for evaluation.

To validate the restoration performance in the mixed noise environment, we simulated six different scenarios for the Washington D.C. Mall HSI data. The noise types are a combination of Gaussian noise, stripe and deadline noise. The specific descriptions of these noisy scenarios as below:

Case 1 (Gaussian + Pepper + Stripe): For the WDC Mall dataset, we add independent Gaussian noise with a standard deviation σ ranging from 0.1 to 0.2 for each band. We also introduce pepper noise for each band with a proportion S ranging from 0.1 to 0.2. Additionally, we randomly select 70% bands and add stripe noise. The number of stripes is randomly generated between 6 and 15.

Case 2 (Gaussian + Pepper + Deadline): In the WDC Mall dataset, we add independent Gaussian noise for each band with a standard deviation σ ranging from 0.1 to 0.2. We also introduce pepper noise to each band with a proportion S ranging from 0.1 to 0.2. Furthermore, we randomly select 40% bands and add 6 to 10 stripes with a width of 1 to 3 pixels as deadline noise.

Case 3 (Gaussian + Pepper + Stripe + Deadline): Relied on Case 2, we randomly select 70% bands and add stripe noise. The number of stripes is randomly generated between 6 and 15.

Case 4 (Gaussian + Pepper + Stripe + Deadline): Like Case 2, we add Gaussian noise, pepper noise, and deadline noise to each band. However, in this case, we increase the proportion of select bands from 40% to 70%.

Case 5 (Gaussian + Pepper + Stripe + Deadline): Extending Case 4, we continue to randomly select 70% bands and add stripe noise. The number of stripes is randomly generated between 6 and 15.

Case 6 (Gaussian + Pepper + Stripe + Deadline): In this case, we add independent Gaussian noise to each band with a standard deviation σ of 0.2. We also introduce pepper noise to each band with a proportion S of 0.2. Additionally, we randomly select 40% bands and add stripe noise with a randomly generated number of stripes between 6 and 15. Furthermore, we randomly select 20% bands and impose with deadline noise. The deadline noise consists of 5 to 10 randomly generated stripes, with the width of 1 to 3 pixels.

To better evaluate the quality of denoised HSI, the performance of all methods in terms of three quantitative evaluation metrics, MP-SNR, MSSIM, and ERGAS, is recorded in Table 1. The optimal metrics are highlighted with **bold** format, while the second-best metrics are indicated with underline format. The following part describes the specific HSI denoising results, enlarged local images, and analysis of the experimental results:

(1) **Case 1:** As shown in Fig. 2, NGMeet could remove random and stripe noise well. However, it exhibits spectral distortion issues. STCR can effectively remove random noise, but it lacks to eliminate coarse stripe noise. LRTV performs well in removing both random noise and stripe noise, while the restored results tend to be over-smoothing and cannot well preserve texture information. Compared to the contrast methods, CTV performs poorly on removing random noise and cannot remove stripe noise. RCTV performs well on removing random noise and achieves a second-best performance on the evaluation metrics.

Table 1

Quantitative evaluation metrics in the simulation experiment on the Washington D.C. Mall HSI data.

Case	Index	Noisy	NGMeet	STCR	LRTV	CTV	RCTV	MAN	QRNN3D	HSID	Proposed
Case 1	MPSNR	10.74	22.93	28.93	25.97	22.19	<u>30.26</u>	20.01	20.12	22.89	31.37
	MSSIM	0.119	0.746	0.807	0.651	0.595	<u>0.888</u>	0.508	0.617	0.653	0.917
	ERGAS	1266	339.9	155.4	206.6	441.1	<u>130.2</u>	648.8	433.1	316.1	113.0
Case 2	MPSNR	11.04	24.29	29.14	26.01	24.81	<u>31.01</u>	20.11	20.34	23.18	32.22
	MSSIM	0.124	0.761	0.837	0.656	0.656	<u>0.895</u>	0.539	0.619	0.675	0.927
	ERGAS	1214	277.7	139.2	209.5	242.6	<u>123.5</u>	592.5	420.6	306.7	102.2
Case 3	MPSNR	10.74	23.09	28.46	25.73	21.78	<u>29.69</u>	20.28	20.67	22.86	31.69
	MSSIM	0.117	0.741	0.848	0.654	0.575	<u>0.874</u>	0.506	0.618	0.653	0.921
	ERGAS	1259	328.5	157.7	218.6	454.9	<u>146.8</u>	614.9	410.6	318.4	107.9
Case 4	MPSNR	11.05	24.45	28.45	25.69	24.35	<u>30.25</u>	20.19	20.51	23.26	32.19
	MSSIM	0.122	0.758	0.832	0.674	0.641	<u>0.883</u>	0.534	0.614	0.664	0.926
	ERGAS	1208	272.4	146.9	218.3	256.4	<u>138.9</u>	625.3	428.6	305.2	103.1
Case 5	MPSNR	10.80	23.36	27.33	25.60	21.83	<u>29.54</u>	19.27	19.69	21.98	31.68
	MSSIM	0.117	0.741	0.808	0.641	0.571	<u>0.866</u>	0.496	0.594	0.635	0.921
	ERGAS	1251	316.3	196.8	224.6	446.8	<u>152.1</u>	595.9	472.7	361.2	108.6
Case 6	MPSNR	9.309	21.64	27.35	24.46	20.66	<u>28.28</u>	18.88	19.04	21.83	29.68
	MSSIM	0.079	0.700	0.808	0.556	0.485	<u>0.826</u>	0.479	0.564	0.613	0.892
	ERGAS	1470	375.6	190.7	246.4	431.9	<u>160.5</u>	625.9	504.2	358.5	138.5
Time	(s)	–	59.32	26.76	76.35	68.81	34.87	1.16	<u>2.59</u>	2.70	38.34

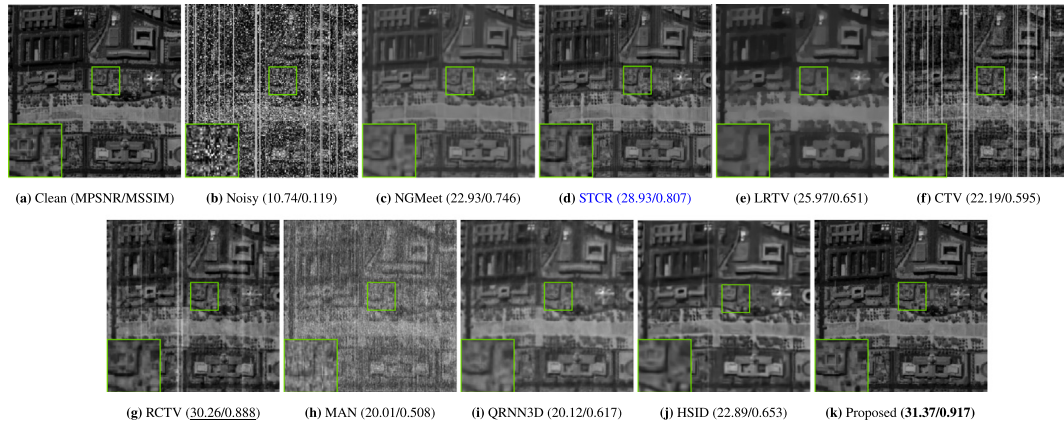


Fig. 2. Denoising result for the 100th band of Washington D.C. Mall HSI data in Case 1.

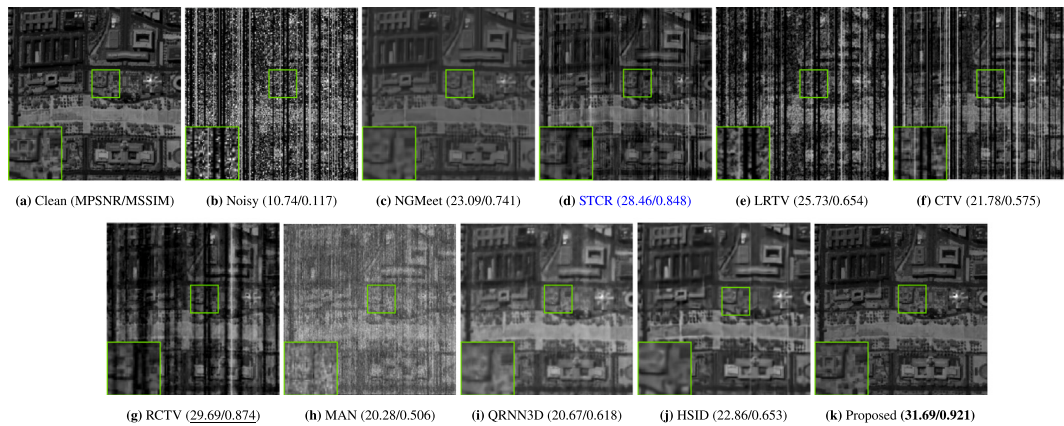


Fig. 3. Denoising result for the 100th band of Washington D.C. Mall HSI data in Case 3.

While RCTV struggles with dense stripe noise. MAN does not show well on removing random and stripe noise, resulting in residual noise. QRNN3D can effectively remove stripe noise. While it exhibits spectral distortion issues and produces over-smoothing restoration results. STCR, CTV, LRTV, and RCTV methods perform poorly on removing dense deadline noise. Among them, RCTV performs better than CTV, LRTV, and LRMR on removing random noise and achieves second-best results

(2) Case 3: To verify the impact of dense deadline noise, we increase the deadline noise in this case. As shown in Fig. 3, NGMeet performs well on removing dense deadline noise. While it exhibits spectral distortion issues and produces over-smoothing restoration results. STCR, CTV, LRTV, and RCTV methods perform poorly on removing dense deadline noise. Among them, RCTV performs better than CTV, LRTV, and LRMR on removing random noise and achieves second-best results

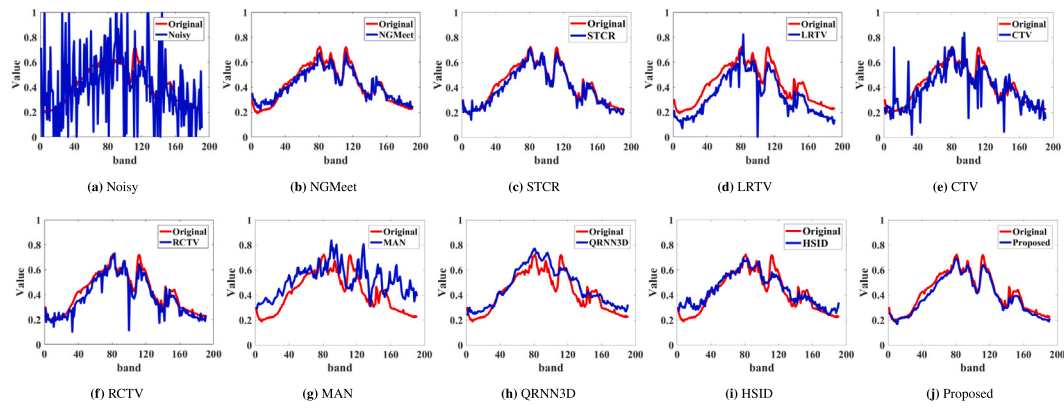


Fig. 4. Spectral curves for position (150, 200) of Washington D.C. Mall HSI data in Case 3.

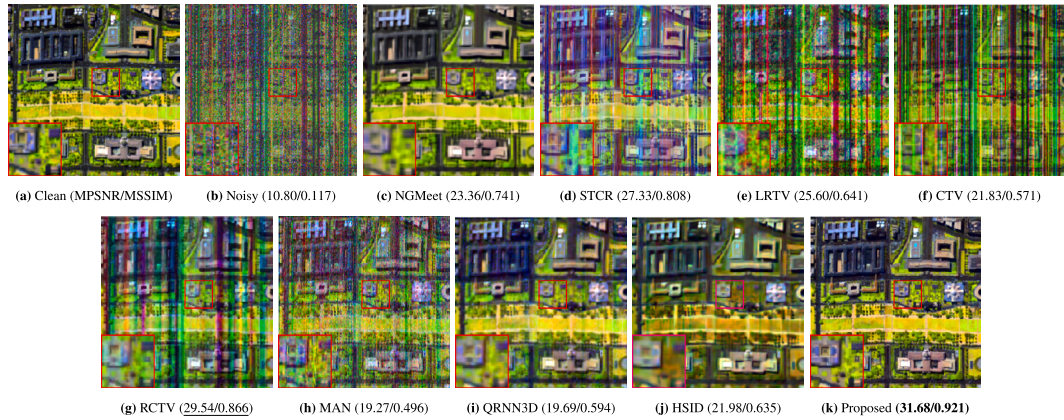


Fig. 5. Pseudo-color denoising result for (100, 68, 10) band of Washington D.C. Mall HSI data in Case 5.

in the evaluation metrics. For the restoration results of MAN, there is residual random noise and dense deadline noise. QRNN3D and HSID exhibit spectral distortion and spatial blurring issues when dealing with dense deadline noise. In Fig. 3(k), the proposed method performs better on removing dense deadline noise. It can also suppress the random noise present in Fig. 3(b).

In order to better verify the spectral fidelity of the proposed method, we present a visual rendering of the spectral curve of pixels (150, 200) in Case 3. As shown in Fig. 4, the spectral curves of NGMeet and STCR could be close to the clean spectral curve. While the noise in the spectral dimension still remains, resulting in a small fluctuation of the spectral curve. LRTV, CTV and CTV are not clean for dense noise, resulting in large fluctuations in the spectral curve after recovery. The three deep learning-based methods, MAN, QRNN3D, and HSID, are less adaptable when faced with complex noise scenarios because they rely too much on a large number of samples to achieve denoising. Therefore, the recovery spectral curve is poorly fitted to the spectral curve of the clean HSI. On the basis of low-rank tensor decomposition, the proposed method considers the spectral information of the whole band, and explores the spectral continuity and consistency through spectral difference. Therefore, the recovered spectral curve is closer to the spectral curve that is not polluted by noise.

(3) Case 5: As shown in Fig. 5, NGMeet, QRNN3D, HSID lose texture detail while removing denser stripe and deadline noise, resulting in the over-smoothing results. STCR and RCTV cannot remove coarse stripe noise very well. LRTV, CTV, and MAN cannot show satisfactory results in removing deadline noise. At the same time, as shown in Fig. 5(k), the proposed method performs the best on removing dense stripe and deadline noise. It also achieves the best results in all three quantitative evaluation metrics.

Based on the data in Table 1, JSSDC-LRTF shows significant improvements in quantitative metrics from Case 1 to Case 6. Particularly, in terms of the MPSNR metric, there is an average enhancement of 1.64 dB, surpassing the comparative methods. This indicates that the proposed method achieves superior results in terms of evaluation metrics.

As shown in Figs. 2 and 3, the proposed method demonstrates superior performance in recovering spatial texture details, compared with other comparative methods. This can be attributed to the utilization of both horizontal and vertical difference constraint in our approach, enabling effective restoration of spatial details in HSI. Furthermore, for the pseudo-color restoration results in Fig. 5 and the spectral curves in Fig. 4, the proposed method exhibits less spectral distortion, compared with other comparative methods. This can be attributed to the incorporation of difference constraint on the spectral dimension, ensuring the preservation of spectral information for the restored image.

In summary, JSSDC-LRTF achieves obvious improvements in both quantitative metrics and visual effects, by simultaneously leveraging difference constraint in both spatial and spectral directions.

4.2. Real experiments

To further prove the denoising effectiveness and practicality of the proposed method for HSI with mixed noise. This section conducts experiments using real HSI data, including EO-1, Urban, and GF-5 datasets. The EO-1 HSI is acquired by the Hyperion hyperspectral imager and has a spatial size of 200×200 and 166 bands. The Urban HSI data is captured by the HYDICE sensor and has a spatial size of 307×307 . The original data consists of 210 bands. After removing several strong noisy bands, 188 bands are retained for the experiments.

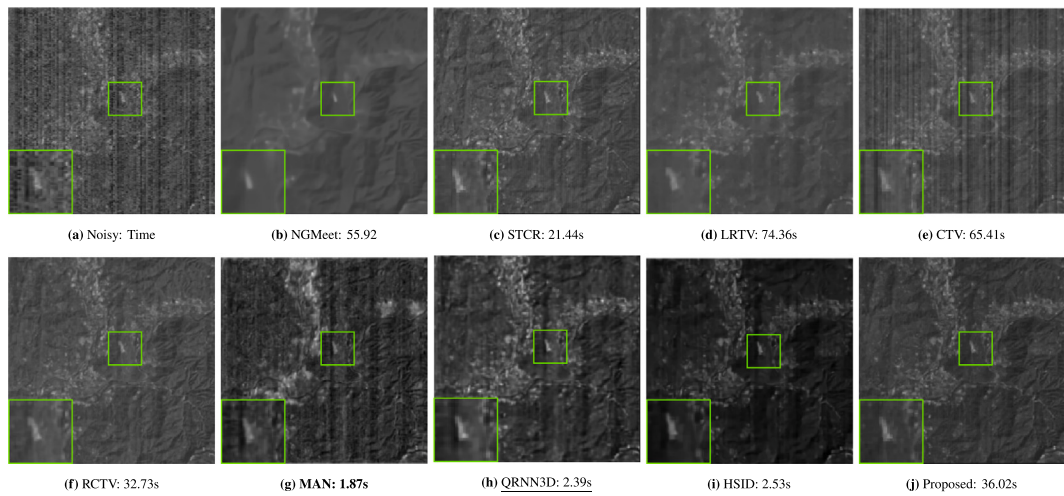


Fig. 6. Denoising result for the 166th band of EO-1 HSI data.

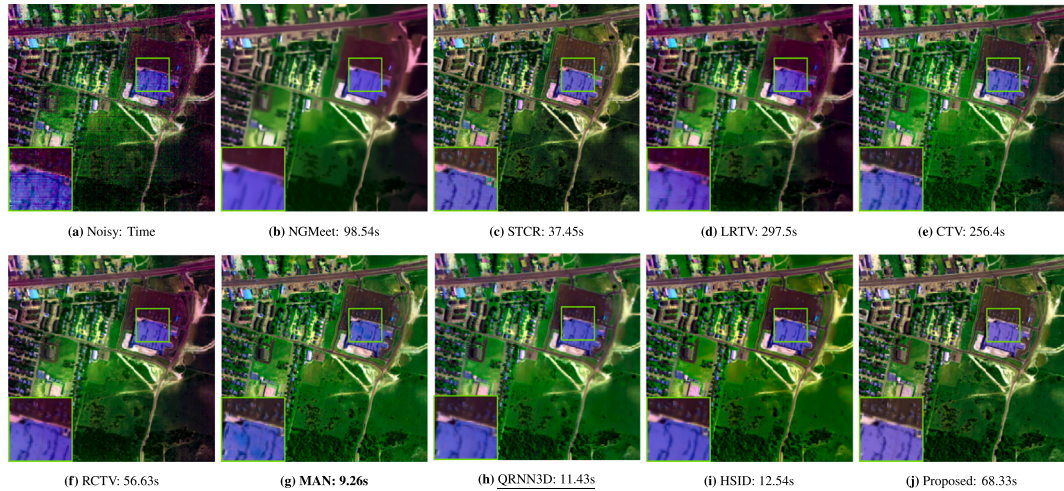


Fig. 7. Pseudo-color denoising result for the (187, 104, 24) band of Urban HSI data.

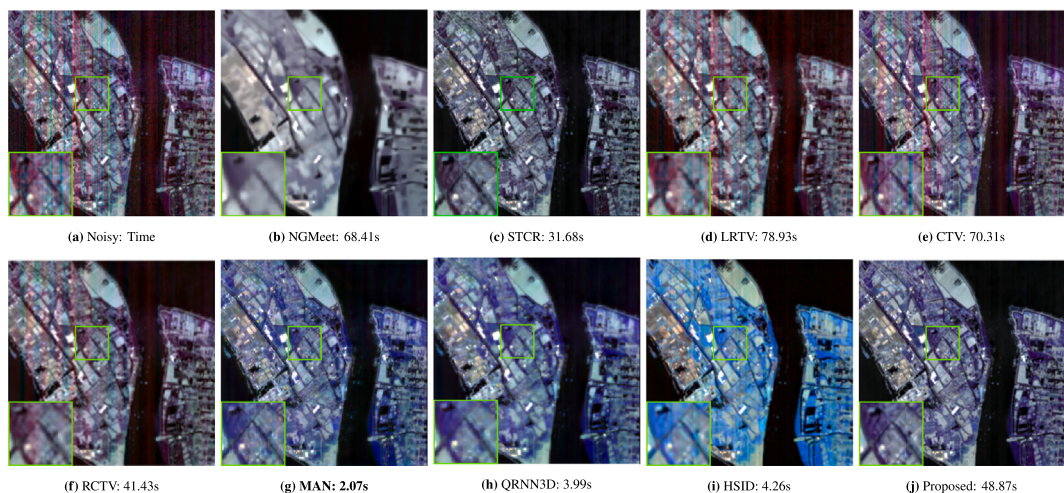


Fig. 8. Pseudo-color denoising result for the (152, 96, 43) band of GF-5 Shanghai HSI data.

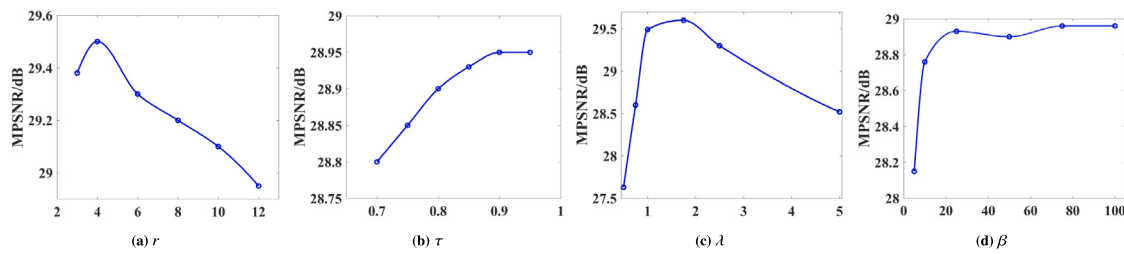


Fig. 9. Sensitivity analysis of model parameters.

The GF-5 HSI data is collected over the Shanghai area and has a spatial size of 300×300 , with 155 bands. This data is corrupted by Gaussian, dense stripe and deadline noise.

The noise intensity and types vary among these HSIs. The specific denoising results and experimental analysis are given as follows.

(1) *EO-1 Data*: Fig. 6 depicts the denoising results for the 166th band of EO-1 HSI data using nine different HSI denoising methods. As shown in Fig. 6(a), it is evident that this HSI is contaminated by Gaussian and stripe noise. Notably, Fig. 6(c)–(e) reveal that STCR, LRTV and CTV exhibit noticeable stripe noise artifacts. NGMeet effectively removes stripe and Gaussian noise in Fig. 6(b), while the denoised result is over-smoothing. RCTV, while removing mixed noise, still exists residual stripe noise artifacts. In the results of MAN and QRNN3D, the stripe noise in Fig. 6(g) and (h) is still obvious. The result of HSID shows spectral distortion. The proposed method effectively removes mixed noise in EO-1 HSI data and demonstrates superior performance, compared with the contrastive approaches.

(2) *Urban Data*: In Fig. 7, the pseudo-color HSI denoising results for the (187, 104, 24) band of the Urban HSI data are presented for comparison using nine different methods. This HSI is primarily affected by random and stripe noise. As shown in Fig. 7(b)–(f), NGMeet, LRTV, and RCTV exhibit residual artifacts. STCR and CTV fail to effectively remove stripe noise, resulting in remaining thin stripe noise artifacts in the denoising results. In Fig. 7(g)–(i), MAN, QRNN3D and HSID could remove both thin stripe noise and random noise. However, MAN suffers from spectral distortion, while QRNN3D and HSID lack clear spatial texture details. In contrast, JSSDC-LRTF not only effectively removes mixed noise on this HSI, but also achieves satisfactory results in preserving spatial details and spectral fidelity.

(3) *GF-5 Data*: Fig. 8 illustrates the pseudo-color denoising results of NGMeet, STCR, LRTV, CTV, RCTV, MAN, QRNN3D, SQAD, and the proposed method for the (152, 96, 43) band of the GF-5 HSI data. This data is primarily contaminated by dense stripe noise and deadline noise, which is more challenging. As shown in Fig. 8, the denoising result of NGMeet exhibits over-smoothing effects. LRTV, CTV and RCTV exist noticeable residual stripe noise and deadline noise. STCR, MAN, QRNN3D and HSID could remove dense deadline and stripe noise, but they appear the spectral distortion in different degrees. Additionally, QRNN3D damages the texture details. In comparison to the contrast methods, the proposed method effectively removes dense stripe noise and deadline noise. Moreover, it can preserve spatial texture details without obvious spectral distortion.

The denoising results of above real HSI datasets demonstrate that JSSDC-LRTF leverages spatial and spectral difference constraint, taking both spatial details and spectral correlations into account. This allows our method to remove high-intensive mixed noise in HSI data more effectively than comparison methods.

4.3. Parameter sensitivity analysis

To analyze the parameters sensitivity of JSSDC-LRTF, we conduct a quantitative analysis on four important parameters in Case 6 of the simulated experiments, as shown in Fig. 9. The four parameters are rank r (characterizes the global spectral correlation of HSI), gradient

Table 2
Quantitative evaluation metrics in the simulation experiments on the CAVE MSI data.

Index	Noisy	NGMeet	STCR	LRTV	CTV	RCTV	Proposed
MPSNR	17.14	33.86	37.81	41.00	32.08	40.47	44.18
MSSIM	0.267	0.814	0.924	0.982	0.914	0.914	0.985
ERGAS	808.6	128.3	82.64	52.27	149.3	57.10	36.31

tensor regularity coefficient τ (plays an important role in excavating spatial-spectral information), sparse noise regularization coefficient λ (trade-off parameter), Gaussian noise regularization coefficient β (trade-off parameter). For different noise scenes, the parameter settings are also different. When most of the noise follows a Gaussian distribution, it is usually possible to set a smaller value of β between [1,10], a larger value of λ between [50,100], and to fine-tune τ between [0,1] (by increasing parameter λ to enhance the removal of sparse noise, while keeping parameter β small to avoid excessive smoothing). For the case where most noise follows a mixed distribution (sparse noise with more Gaussian noise with less), we can set λ to a smaller value between [1,10], β to a larger value between [50,100], and then fine-tune τ between [0,1] (by increasing the parameter β to avoid ignoring Gaussian noise. The parameter λ is smaller to finely remove these significant sparse noises). However, in real scenes, the noise distribution of HSI is usually mixed and dense, so this paper pays more attention to the mixed noise scene. For all scenes in this paper (which are all mixed noise), the four parameters r , τ , β and λ are set between [3,6], [0,1], [50,100] and [1,10] respectively for fine tuning, to achieve the best noise reduction effects. When the noise is denser, we could narrow the parameter range to [3,6], [0.8, 0.95], [1,2.5], [70,85], respectively (taking Case 6 as an example).

4.4. Multispectral image experiments

We select a scene in the CAVE dataset and add mixed noise (Gaussian + salt and pepper + deadline + stripe) to verify the effectiveness of the proposed method for noise removal in multispectral images. The specific indicators and visuals are shown below (see Fig. 10 and Table 2).

It could be observed that compared with the SOTA method, the proposed method can not only remove the mixed noise of the multispectral image, but also maintain the clear texture details.

4.5. Classification results

Generally, HSI denoising is benefit for classification, through removing the polluted noise in HSI. To ulteriorly validate the availability of different HSI restoration methods, classification results before and after HSI denoising are carried out in this subsection.

Based on supervised SVM strategy, ground-truth classes are utilized for verifying the classification precision, as portrayed in Fig. 11. The classification accuracy indexes (OA and kappa coefficient) are listed in Table 3. These HSI classification results for Pavia University data are displayed in Fig. 11. Compared with noisy HSI, different HSI denoising methods contribute to subsequent classification tasks. This

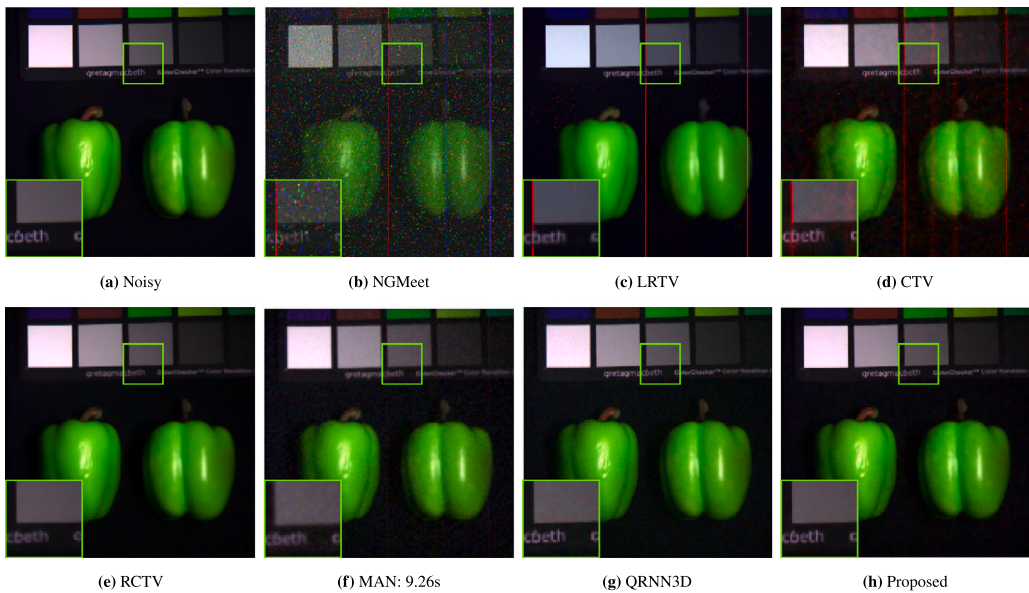


Fig. 10. Pseudo-color denoising result for the (14, 26, 4) band of CAVE MSI data.

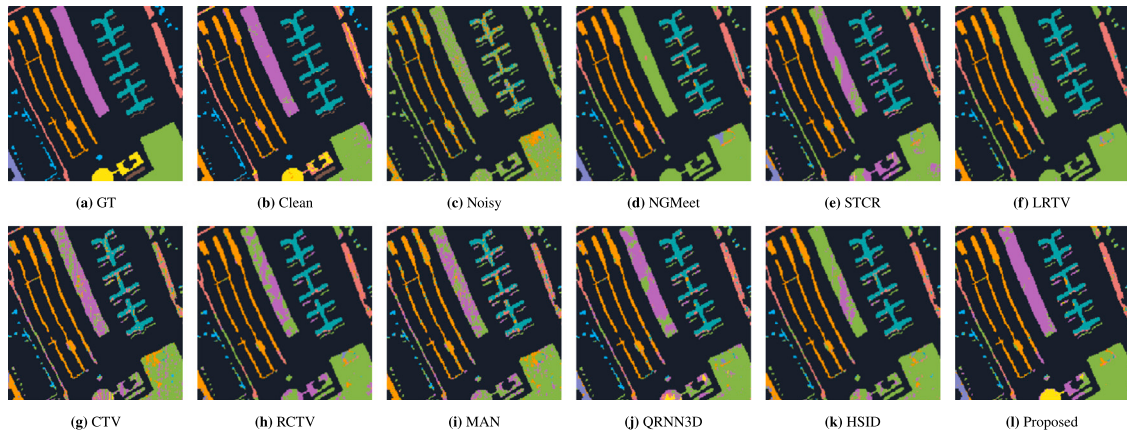


Fig. 11. HSI classification results for Pavia University data before and after HSI denoising.

Table 3
HSI classification accuracy indexes for Pavia University HSI data before and after denoising.

Index	Clean	Noisy	NGMeet	STCR	LRTV	CTV	RCTV	MAN	QRNN3D	HSID	Proposed
OA	0.886	0.394	0.725	0.799	0.712	0.727	0.775	0.699	0.808	0.729	0.827
Kappa	0.863	0.205	0.622	0.704	0.604	0.665	0.693	0.596	0.721	0.632	0.787

also validates the effectiveness and meaning for HSI denoising. From the classification accuracy, kappa coefficient and visual classification effect of the quantitative indexes, compared with other methods, the proposed method effectively improves the accuracy of the HSI classification task after removing mixed noise. Besides, and the classification effects of the proposed method are the best.

5. Conclusion

For HSI mixed noise removal, this paper proposes a jointly spatial and spectral difference constraint with low-rank tensor factorization model. The developed approach effectively removes the mixed noise in HSI by leveraging the tensor's intrinsic structural information, while preserving its three-dimensional structure. Experiments on both simulated and real data confirm the excellence of the proposed method, particularly for high-intensive mixed noise. In the future, we will construct a joint noise model (Gaussian and sparse noise) to characterize

the noise characteristics of hyperspectral and multispectral images, by analyzing the spatial and spectral correlations of noise. the tensor decomposition strategy will be used to decompose the HSI into low-rank components and sparse noise components, so as to achieve denoising and provide a theoretical basis for the multi-source image denoising algorithm.

CRediT authorship contribution statement

Qiang Zhang: Writing – review & editing, Writing – original draft, Validation, Methodology. **Yaming Zheng:** Writing – review & editing, Writing – original draft, Methodology, Data curation. **Yushuai Dong:** Writing – review & editing, Software, Resources. **Chunyan Yu:** Writing – review & editing, Resources. **Qiangqiang Yuan:** Writing – review & editing, Funding acquisition.

Declaration of competing interest

The authors declare the following financial interests/personal relationships which may be considered as potential competing interests: Qiang Zhang reports financial support was provided by National Natural Science Foundation of China. If there are other authors, they declare that they have no known competing financial interests or personal relationships that could have appeared to influence the work reported in this paper.

Acknowledgments

This work was supported in part by the Open Fund of State Key Laboratory of Remote Sensing Science (Grant No. OFSLRSS202301), in part by the National Natural Science Foundation of China under Grant 62401095, in part by the Fundamental Research Funds for the Central Universities under Grant 3132025262, in part by the Dalian Science and Technology Talent Innovation Supporting Project under Grant 2024RQ028, and in part by the China Postdoctoral Science Foundation under Grant 2023M740460.

Data availability

Data will be made available on request.

References

- Ahmad, I., Farooque, G., Liu, Q., Hadi, F., Xiao, L., 2024. Mtsenet: Multiscale spectral-spatial transformer with squeeze and excitation network for hyperspectral image classification. *Eng. Appl. Artif. Intell.* 134, 108669.
- Beck, A., Teboulle, M., 2009. Fast gradient-based algorithms for constrained total variation image denoising and deblurring problems. *IEEE Trans. Image Process.* 18 (11), 2419–2434.
- Chen, Y., Cao, X., Zhao, Q., Meng, D., Xu, Z., 2018b. Denoising hyperspectral image with non-i.i.d. Noise structure. *IEEE Trans. Cybern.* 48 (3), 1054–1066.
- Chen, C., Jiang, F., Yang, C., Rho, S., Shen, W., Liu, S., Liu, Z., 2018a. Hyperspectral classification based on spectral-spatial convolutional neural networks. *Eng. Appl. Artif. Intell.* 68, 165–171.
- Dian, R., Li, S., Kang, X., 2020. Regularizing hyperspectral and multispectral image fusion by CNN denoiser. *IEEE Trans. Neural Netw. Learn. Syst.* 32 (3), 1124–1135.
- Fernandes, S., Fanaee-T, H., Gama, J., 2020. Normo: A new method for estimating the number of components in CP tensor decomposition. *Eng. Appl. Artif. Intell.* 96, 103926.
- Fu, X., Guo, Y., Xu, M., Jia, S., 2023. Hyperspectral image denoising via robust subspace estimation and group sparsity constraint. *IEEE Trans. Geosci. Remote Sens.* 61, 1–16.
- Gao, Q., Xie, F., Huang, D., Jin, C., 2022. Spectral and spatial reduction of hyperspectral image guided by data reconstruction and superpixels. *Eng. Appl. Artif. Intell.* 111, 104803.
- He, C., Wei, Y., Guo, K., Han, H., 2024. Removal of mixed noise in hyperspectral images based on subspace representation and nonlocal low-rank tensor decomposition. *Sensors* (14248220) 24 (2).
- He, W., Yao, Q., Li, C., Yokoya, N., Zhao, Q., 2019. Non-local meets global: An integrated paradigm for hyperspectral denoising. *IEEE Trans. Pattern Anal. Mach. Intell.* 6868–6877.
- He, W., Zhang, H., Zhang, L., Shen, H., 2015. Total-variation-regularized low-rank matrix factorization for hyperspectral image restoration. *IEEE Trans. Geosci. Remote Sens.* 54 (1), 178–188.
- Huang, J., Chen, K.-H., Wang, J.-J., Yan, W., 2024. Hyperspectral image denoising via weighted double sparsity total variation and low-rank representation. *Inverse Probl. Imaging.*
- Jiang, T.-X., Zhuang, L., Huang, T.-Z., Zhao, X.-L., Bioucas-Dias, J.M., 2022. Adaptive hyperspectral mixed noise removal. *IEEE Trans. Geosci. Remote Sens.* 60, 1–13.
- Kerekes, J.P., Baum, J.E., 2003. Hyperspectral imaging system modeling. *Linc. Lab. J.* 14 (1), 117–130.
- Krishnan, D., Fergus, R., 2009. Fast image deconvolution using hyper-Laplacian priors. In: *Proc. Adv. Neural Inf. Process. Syst.* Vol. 22.
- Lai, Z., Fu, Y., 2023. Mixed attention network for hyperspectral image denoising. In: *IEEE Conf. Comp. Vis. Pattern Recogn.*
- Li, L., Song, M., Zhang, Q., Dong, Y., 2023. Hyperspectral denoising via global variation and local structure low-rank model. *IEEE Trans. Geosci. Remote Sens.* 61, 1–13.
- Luo, Y.-S., Zhao, X.-L., Jiang, T.-X., Zheng, Y.-B., Chang, Y., 2021. Hyperspectral mixed noise removal via spatial-spectral constrained unsupervised deep image prior. *IEEE J. Sel. Top. Appl. Earth Obs. Remote. Sens.* 14, 9435–9449.
- Ma, T.-H., Xu, Z., Meng, D., 2020. Remote sensing image denoising via low-rank tensor approximation and robust noise modeling. *Remote. Sens.* 12 (8).
- Miao, Y.-C., Zhao, X.-L., Fu, X., Wang, J.-L., Zheng, Y.-B., 2022. Hyperspectral denoising using unsupervised disentangled spatiotemporal deep priors. *IEEE Trans. Geosci. Remote Sens.* 60, 1–16.
- Pan, B., Li, C., Che, H., 2024. Error-robust multi-view subspace clustering with nonconvex low-rank tensor approximation and hyper-Laplacian graph embedding. *Eng. Appl. Artif. Intell.* 133, 108274.
- Pan, E., Ma, Y., Mei, X., Fan, F., Huang, J., Ma, J., 2022. SQAD: Spatial-spectral quasi-attention recurrent network for hyperspectral image denoising. *IEEE Trans. Geosci. Remote Sens.* 60, 1–14.
- Peng, J., Wang, H., Cao, X., Liu, X., Rui, X., Meng, D., 2022a. Fast noise removal in hyperspectral images via representative coefficient total variation. *IEEE Trans. Geosci. Remote Sens.* 60, 1–17.
- Peng, J., Wang, Y., Zhang, H., Wang, J., Meng, D., 2022b. Exact decomposition of joint low rankness and local smoothness plus sparse matrices. *IEEE Trans. Pattern Anal. Mach. Intell.* 45 (5), 5766–5781.
- Peng, J., Xie, Q., Zhao, Q., Wang, Y., Yee, L., Meng, D., 2020. Enhanced 3DTV regularization and its applications on HSI denoising and compressed sensing. *IEEE Trans. Image Process.* 29, 7889–7903.
- Qin, W., Wang, H., Zhang, F., Wang, J., Luo, X., Huang, T., 2022. Low-rank high-order tensor completion with applications in visual data. *IEEE Trans. Image Process.* 31, 2433–2448.
- Rudin, L.I., Osher, S., Fatemi, E., 1992. Nonlinear total variation based noise removal algorithms. *Phys. D, Nonlinear Phenom.* 60 (1–4), 259–268.
- Su, Y., Zhu, H., Wong, K.-C., Chang, Y., Li, X., 2023. Hyperspectral image denoising via weighted multidirectional low-rank tensor recovery. *IEEE Trans. Cybern.* 53 (5), 2753–2766.
- Sun, L., Cao, Q., Chen, Y., Zheng, Y., Wu, Z., 2023a. Mixed noise removal for hyperspectral images based on global tensor low-rankness and nonlocal SVD-aided group sparsity. *IEEE Trans. Geosci. Remote Sens.* 61, 1–17.
- Sun, L., He, C., 2021. Hyperspectral image mixed denoising using difference continuity-regularized nonlocal tensor subspace low-rank learning. *IEEE Geosci. Remote. Sens. Lett.* 19, 1–5.
- Sun, L., He, C., Zheng, Y., Wu, Z., Jeon, B., 2023b. Tensor cascaded-rank minimization in subspace: A unified regime for hyperspectral image low-level vision. *Trans. Image Process.* 32, 100–115.
- Wang, F., Li, J., Yuan, Q., Zhang, L., 2022. Local-global feature-aware transformer based residual network for hyperspectral image denoising. *IEEE Trans. Geosci. Remote Sens.* 60, 1–19.
- Wang, H., Peng, J., Qin, W., Wang, J., Meng, D., 2023b. Guaranteed tensor recovery fused low-rankness and smoothness. *IEEE Trans. Pattern Anal. Mach. Intell.* 45 (9), 10990–11007.
- Wang, Q., Wu, Z., Jin, J., Wang, T., Shen, Y., 2018. Low rank constraint and spatial spectral total variation for hyperspectral image mixed denoising. *Signal Process.* 142, 11–26.
- Wang, C., Zhao, X.-L., Zhang, H., Li, B.-Z., Ding, M., 2023a. Hyperspectral image mixed noise removal via nonlinear transform-based block-term tensor decomposition. *IEEE Geosci. Remote. Sens. Lett.* 20, 1–5.
- Wang, C., Zhu, F., Zhu, B., Zhang, Q., Ma, H., 2024. Reference-based super-resolution reconstruction of remote sensing images based on a coarse-to-fine feature matching transformer. *Eng. Appl. Artif. Intell.* 135, 108787.
- Wei, K., Fu, Y., Huang, H., 2020. 3-D quasi-recurrent neural network for hyperspectral image denoising. *IEEE Trans. Neural Netw. Learn. Syst.* 32 (1), 363–375.
- Wu, Y., Xu, W., Zheng, L., 2024. Hyperspectral image mixed noise removal via double factor total variation nonlocal low-rank tensor regularization. *Remote. Sens.* 16, 1686.
- Xiao, Y., Yuan, Q., He, J., Zhang, Q., Sun, J., Su, X., Wu, J., Zhang, L., 2022. Space-time super-resolution for satellite video: A joint framework based on multi-scale spatial-temporal transformer. *Int. J. Appl. Earth Obs. Geoinf.* 108, 102731.
- Xiao, Y., Yuan, Q., Jiang, K., He, J., Wang, Y., Zhang, L., 2023a. From degrade to upgrade: Learning a self-supervised degradation guided adaptive network for blind remote sensing image super-resolution. *Inf. Fusion* 96, 297–311.
- Xiao, Y., Yuan, Q., Zhang, Q., Zhang, L., 2023b. Deep blind super-resolution for satellite video. *IEEE Trans. Geosci. Remote Sens.* 61, 1–16.
- Xiong, F., Zhou, J., Tao, S., Lu, J., Zhou, J., Qian, Y., 2022a. SMDS-Net: Model guided spectral-spatial network for hyperspectral image denoising. *IEEE Trans. Image Process.* 31, 5469–5483.
- Xiong, F., Zhou, J., Zhao, Q., Lu, J., Qian, Y., 2022b. MAC-Net: Model-aided nonlocal neural network for hyperspectral image denoising. *IEEE Trans. Geosci. Remote Sens.* 60, 1–14.
- Xu, J., Li, K., Li, Z., Chong, Q., Xing, H., Xing, Q., Ni, M., 2024. Fuzzy graph convolutional network for hyperspectral image classification. *Eng. Appl. Artif. Intell.* 127, 107280.
- Yao, J., Meng, D., Zhao, Q., Cao, W., Xu, Z., 2019. Nonconvex-sparsity and nonlocal-smoothness-based blind hyperspectral unmixing. *IEEE Trans. Image Process.* 28 (6), 2991–3006.
- Yu, C., Huang, J., Song, M., Wang, Y., Chang, C.I., 2022a. Edge-inferring graph neural network with dynamic task-guided self-diagnosis for few-shot hyperspectral image classification. *IEEE Trans. Geosci. Remote Sens.* 60, 1–13.

- Yu, S., Seo, D., Paik, J., 2023. Haze removal using deep convolutional neural network for Korea multi-purpose satellite-3A (KOMPSAT-3A) multispectral remote sensing imagery. *Eng. Appl. Artif. Intell.* 123, 106481.
- Yu, C., Zhao, X., Gong, B., Hu, Y., Song, M., Yu, H., Chang, C.-I., 2024. Distillation-constrained prototype representation network for hyperspectral image incremental classification. *IEEE Trans. Geosci. Remote Sens.* 62, 1–14.
- Yu, C., Zhou, S., Song, M., Chang, C.-I., 2022b. Semisupervised hyperspectral band selection based on dual-constrained low-rank representation. *IEEE Geosci. Remote. Sens. Lett.* 19, 1–5.
- Yuan, Q., Zhang, Q., Li, J., Shen, H., Zhang, L., 2019. Hyperspectral image denoising employing a spatial-spectral deep residual convolutional neural network. *IEEE Trans. Geosci. Remote Sens.* 57 (2), 1205–1218.
- Zhang, H., Chen, H., Yang, G., Zhang, L., 2021a. LR-Net: Low-rank spatial-spectral network for hyperspectral image denoising. *IEEE Trans. Image Process.* 30, 8743–8758.
- Zhang, Q., Dong, Y., Yuan, Q., Song, M., Yu, H., 2023a. Combined deep priors with low-rank tensor factorization for hyperspectral image restoration. *IEEE Geosci. Remote. Sens. Lett.* 20, 1–5.
- Jie Zhang, C., wei Liu, J., 2024. Change detection with incorporating multi-constraints and loss weights. *Eng. Appl. Artif. Intell.* 133, 108163.
- Zhang, L., Qian, Y., Han, J., Duan, P., Ghamisi, P., 2022a. Mixed noise removal for hyperspectral image with l_0-l_{1-2} -stv regularization. *IEEE J. Sel. Top. Appl. Earth Obs. Remote. Sens.* 15, 5371–5387.
- Zhang, F., Yang, G., Xue, J.-H., 2020a. Hyperspectral image denoising based on low-rank coefficients and orthonormal dictionary. *Signal Process.* 177, 107738.
- Zhang, Q., Yuan, Q., Li, J., Li, Z., Shen, H., Zhang, L., 2020b. Thick cloud and cloud shadow removal in multitemporal imagery using progressively spatio-temporal patch group deep learning. *ISPRS J. Photogramm. Remote Sens.* 162, 148–160.
- Zhang, Q., Yuan, Q., Li, J., Liu, X., Shen, H., Zhang, L., 2019. Hybrid noise removal in hyperspectral imagery with a spatial-spectral gradient network. *IEEE Trans. Geosci. Remote Sens.* 57 (10), 7317–7329.
- Zhang, Q., Yuan, Q., Li, J., Sun, F., Zhang, L., 2020c. Deep spatio-spectral Bayesian posterior for hyperspectral image non-iid noise removal. *ISPRS J. Photogramm. Remote Sens.* 164, 125–137.
- Zhang, Q., Yuan, Q., Li, Z., Sun, F., Zhang, L., 2021c. Combined deep prior with low-rank tensor SVD for thick cloud removal in multitemporal images. *ISPRS J. Photogramm. Remote Sens.* 177, 161–173.
- Zhang, Q., Yuan, Q., Li, J., Wang, Y., Sun, F., Zhang, L., 2021b. Generating seamless global daily AMSR2 soil moisture (SGD-SM) long-term products for the years 2013–2019. *Earth Syst. Sci. Data* 13 (3), 1385–1401.
- Zhang, Q., Yuan, Q., Li, J., Yang, Z., Ma, X., 2018. Learning a dilated residual network for SAR image despeckling. *Remote. Sens.* 10 (2), 196.
- Zhang, Q., Yuan, Q., Song, M., Yu, H., Zhang, L., 2022b. Cooperated spectral low-rankness prior and deep spatial prior for HSI unsupervised denoising. *IEEE Trans. Image Process.* 31, 6356–6368.
- Zhang, Q., Zheng, Y., Yuan, Q., Song, M., Yu, H., Xiao, Y., 2023b. Hyperspectral image denoising: From model-driven, data-driven, to model-data-driven. *IEEE Trans. Neural Netw. Learn. Syst.*
- Zheng, J., Qin, M., Xu, H., Feng, Y., Chen, P., Chen, S., 2021. Tensor completion using patch-wise high order Hankelization and randomized tensor ring initialization. *Eng. Appl. Artif. Intell.* 106, 104472.
- Zhuang, L., Ng, M.K., 2023. FastHyMix: Fast and parameter-free hyperspectral image mixed noise removal. *IEEE Trans. Neural Netw. Learn. Syst.* 34 (8), 4702–4716.